Dicle University
Journal of Engineering
https://dergipark.org.tr/tr/pub/dumf
duje.dicle.edu.tr

Research Article

Balancing Mixing Enhancement and Momentum Conservation in Supersonic Ejectors: A Numerical Investigation of Sinusoidal Mixing Chamber Geometry

Hayati TÖRE[1*]

[1] Hitit University, Mechanical Engineering Department, hayatitore@hitit.edu.tr, Orcid No: 0000-0002-1855-9182

ARTICLE INFO

Article history:

Received 19 January 2026
Received in revised form 30 June 2026
Accepted 30 June 2026
Available online 12 July 2026

Keywords:

Supersonic Ejector, Sinusoidal Mixing Chamber, CFD, Turbulent Kinetic Energy (TKE), R134a Real-Gas Model, Shock–Vortex Interaction.

Doi: 10.24012/dumf.1866561

* Corresponding author

ABSTRACT

This study presents a comprehensive three dimensional Computational Fluid Dynamics investigation into the impact of sinusoidal wall structures within the mixing chamber on the flow physics and performance of an R134a driven supersonic ejector. By preserving the mean cross sectional area across the sinusoidal configurations, the study reduces the influence of global flow area variation and enables the effects of dimensionless amplitude and wavelength on wall induced flow phenomena to be interpreted more clearly. The numerical framework integrates a real gas equation of state derived from the NIST REFPROP database with the k omega Shear Stress Transport turbulence model to resolve the interactions between shocks, shear layers, and turbulent fluctuations. The results demonstrate that sinusoidal modulation reshapes the internal flow field by generating strong streamwise vortices and shock boundary layer interactions, which accelerate the collapse of the supersonic potential core. At a constant dimensionless wavelength of 1.5, increasing the amplitude from 0.01 to 0.03 amplifies turbulence kinetic energy production. However, this intensified mixing reduces the entrainment ratio because primary jet momentum is dissipated into turbulent fluctuations. Conversely, increasing the wavelength at a fixed amplitude of 0.02 redistributes turbulence energy over a broader axial extent, enabling a more effective balance between mixing enhancement and momentum conservation. A dimensionless forcing parameter is introduced to interpret this balance. Case 5 provides the highest entrainment ratio among the sinusoidal configurations, whereas Case 6 represents a more controlled and spatially distributed mixing regime. These findings provide a scalable interpretation framework and show that passive wall modulation can control the balance between mixing enhancement and entrainment loss in supersonic ejectors.

Introduction

The increasing global energy demand and the necessity to combat climate change have heightened interest in systems capable of efficiently converting low-grade heat sources and waste energy [1], [2]. In this context, supersonic ejectors-characterized by their lack of moving parts, low maintenance costs, and high reliability-play a critical role across a wide range of applications, including refrigeration, aerospace, fuel cells, and chemical processes [3], [4], [5]. The fundamental operating principle of an ejector relies on using the momentum of a high-pressure primary flow to entrain a low-pressure secondary flow and compress the resulting mixture to a specific pressure level [6], [7], [8]. However, the efficiency of the system depends heavily on complex flow physics, shock wave interactions, and the fluid mixing process. In the literature, the primary parameters determining ejector performance are defined as the entrainment ratio (ER), critical back pressure, and compression ratio. Geometric effects on these parameters have focused particularly on the nozzle exit position (NXP) and mixing chamber design. For instance, Cai et al. (2011) [9] demonstrated that nozzle position and throat diameter have optimal values for the entrainment ratio. Similarly, Kracik and Dvorak (2016) [10] experimentally and numerically verified the direct impact of NXP variations on the operational characteristics of the ejector. To improve the mixing process, Srikrishnan et al. (1996) [4] revealed that petal-type nozzles provide faster mixing than conventional conical nozzles, while Yang et al. (2012) [11] examined the effects of different nozzle structures on vortex formation and mixing quality.

The stability of the flow within the ejector is closely related to the transition between "on-design" and "off-design" operating regimes [12], [13]. Lamberts et al. (2018) [12] numerically and experimentally proved the "Fabri-choking" phenomenon, defined as the secondary flow reaching sonic velocity in an aerodynamic throat. The destructive effects of shock wave structures on performance were addressed by Dvorak and Safarik (2005) [14] within the framework of transonic instabilities, while Zou et al. (2012) [15] visualized shock wave movements during the startup process using the Schlieren method. Additionally, Dong et al. (2012) [16] evaluated the sensitivity of turbulence models in predicting the shock-mixing layer, identifying the k-omega SST model as the most suitable for estimating pressure profiles. Geometric innovations continue to push the boundaries of ejector technology. Shan et al. (2018) [17] and Yang et al. (2025) [18] investigated the potential of multi-nozzle "piccolo-tube" designs in non-uniform mixing chambers to increase cooling capacity. Aiming to enhance mixing performance through passive methods, Talebiyan et al. (2025) [19] reported that aerodynamic cavities added to the mixing chamber could increase the entrainment ratio by up to 163%, particularly at high back pressures. On the other hand, Dandani et al. (2018) [20] emphasized the enhancing effects of transverse micro-jets, and Li et al. (2025) [21] highlighted the impact of annular designs on mixing layer thickness.

Modeling fluid properties is vital for the accuracy of ejector analysis. Cai and He (2013) [22] stated that the ideal gas assumption is insufficient for high-pressure steam flows and that the use of the IAPWS-IF97 real gas model is mandatory. While Vojta et al. (2018) [23] examined the performance of R32 fluid in ejectors, Ariafar et al. (2018) [24] showed that wet steam models yield different results than ideal gas models due to condensation effects. Furthermore, Zheng et al. (2022a) [25] performed optimization of phase change and flow distribution in CO_2 ejectors. The effects of wall roughness and friction losses should also not be ignored; Zhang et al. (2018) [26] and Brezgin et al. (2017) [27] proved that incorporating friction factors into calculations reduces the discrepancy with experimental data to below 10%. Kracik and Dvorak (2023) [28] suggested that wall roughness could trigger the compound choking mechanism.

In modern ejector studies, as noted by Al-Doori et al. (2025) [29], artificial intelligence and machine learning algorithms have opened a new horizon for predicting complex gas dynamics. However, there is still a need for in-depth information regarding the performance of ejectors, especially in micro-scale electronic cooling [30] and pre-cooled systems [31]. Despite comprehensive reviews by researchers such as Majchrzyk et al. (2022) [32] and Zheng et al. (2022b) [25], the relationship between mixing layer development in irregular geometries and local flow phenomena has not been fully established [25], [32].

The fundamental motivation for this research stems from the pressing need to enhance the efficiency of low-grade heat recovery systems through advanced passive mixing techniques, which remain critical for sustainable refrigeration and industrial processes. Although the literature has explored various geometric innovations such as aerodynamic cavities and multi-nozzle designs, a definitive understanding of how periodic wall modulations influence the intricate interplay between shock structures and local turbulence production is currently missing. Accordingly, the primary objective of this study is to fill this gap in the literature by numerically investigating the effects of sinusoidal wave structures with different amplitudes and wavelengths on the mixing chamber walls of a supersonic ejector using Computational Fluid Dynamics. In this context, the simulations are designed across a Baseline model and six different configurations: Cases 1–3 (varying amplitudes at a fixed wavelength) and Cases 4–6 (varying wavelengths at a fixed amplitude). This study introduces a sinusoidal mixing chamber design in which the mean cross sectional area is preserved across the investigated configurations. This approach reduces the influence of global flow area variation while retaining the local curvature, wall slope, wetted surface effects, and wall induced vortex generation that constitute the geometric forcing mechanism. The originality of this work lies in the introduction of a dimensionless forcing parameter that serves as a compact first order index for interpreting the balance between mixing intensification and primary jet momentum conservation. This parameter is not treated as a unique similarity parameter, because amplitude, wavelength, wall slope, and curvature may produce different local flow responses even at comparable forcing levels. By elucidating the physical mechanisms behind shock vortex interactions in wavy geometries, this research clarifies how sinusoidal wall forcing modifies ejector mixing, momentum redistribution, and entrainment behavior under the investigated operating condition.

2. Methodology

The numerical methodology employed in this research is founded upon established best practices for compressible flow CFD in supersonic ejectors. The governing equations, real-gas thermodynamics, turbulence modeling, and performance metrics are detailed in the following subsections. The one dimensional ejector relations reported by Garcia del Valle et al. [33] and Huang et al. [34] are introduced only as theoretical background for primary nozzle expansion and ejector performance interpretation. All three dimensional CFD simulations were performed using Siemens Simcenter FloEFD 2025 [36] in a CAD integrated computational environment.

For the supersonic expansion within the nozzle, the mass flow rate ($\dot{m}_p$) at the throat and the nozzle exit Mach number (M_{ane}) for the primary flow are expressed via isentropic relations:

$$\dot{m}_p = A_t\, P_g \sqrt{\frac{\gamma}{RT_g}\left(\frac{2}{\gamma+1}\right)^{\frac{\gamma+1}{\gamma-1}}} \tag{1}$$

$$\frac{A_{ne}}{A_t} = \frac{1}{M_{ane}}\left[\frac{2}{\gamma+1}\left(1+\frac{\gamma-1}{2}M_{ane}^2\right)\right]^{\frac{\gamma+1}{2(\gamma-1)}} \tag{2}$$

Where A_t is the nozzle throat area, A_{ne} is the nozzle exit area, P_g and T_g represent the primary flow stagnation pressure and temperature, γ is the specific heat ratio, and R is the gas constant. These ideal gas isentropic relations are presented only to describe the one dimensional reference framework and were not used to replace the REFPROP based real gas property evaluation in the three dimensional CFD simulations. Therefore, the one dimensional relations were not used to impose the final ejector performance values, and the reported entrainment ratios were obtained directly from the three dimensional REFPROP based CFD calculations.

2.1. Governing Equations

The supersonic, high-gradient, and turbulent flow within the ejector is modeled by solving the Reynolds-Averaged Navier-Stokes (RANS) forms of the conservation of mass, momentum, and energy equations. The Reynolds stress term in Equation (4) represents the additional transport contributed to momentum by turbulent velocity fluctuations; this effect is modeled as a function of eddy viscosity.

Continuity equation:

$$\frac{\partial \bar{\rho}}{\partial t} + \frac{\partial}{\partial x_i}(\bar{\rho}\tilde{u}_i) = 0 \tag{3}$$

Conservation of Momentum:

$$\frac{\partial}{\partial t}(\bar{\rho}\tilde{u}_i) + \frac{\partial}{\partial x_j}(\bar{\rho}\tilde{u}_i\tilde{u}_j) = -\frac{\partial \bar{p}}{\partial x_i} + \frac{\partial}{\partial x_j}\left[\bar{\tau}_{ij} - \overline{\rho u_i'' u_j''}\right] \tag{4}$$

$$\bar{\tau}_{ij} = \mu\left(\frac{\partial \tilde{u}_i}{\partial x_j} + \frac{\partial \tilde{u}_j}{\partial x_i} - \frac{2}{3}\delta_{ij}\frac{\partial \tilde{u}_k}{\partial x_k}\right) \tag{5}$$

Conservation of Energy:

Given that abrupt energy transformations across normal and oblique shocks in supersonic ejectors directly influence pressure recovery and mixing, employing the total enthalpy form of the energy equation is particularly suitable for accurately representing these processes [35].

$$\frac{\partial}{\partial t}(\bar{\rho}\tilde{H}) + \frac{\partial}{\partial x_j}(\bar{\rho}\tilde{u}_j\tilde{H}) = \frac{\partial}{\partial x_j}\left[\left(\frac{\mu}{Pr} + \frac{\mu_t}{Pr_t}\right)\frac{\partial \tilde{h}}{\partial x_j}\right] + \frac{\partial}{\partial x_j}\left[\tilde{u}_i(\bar{\tau}_{ij} - \rho \overline{u_i'' u_j''})\right] \tag{6}$$

2.2. Real-Gas Equation of State (EOS)

Since the ejector flow under investigation involves high-speed compressible jets, intense pressure gradients, and local shock structures, the variations in temperature, pressure, and density for R134a lead to significant deviations from ideal gas behavior. Consequently, to prevent inaccurate predictions of critical parameters such as density, enthalpy, and the speed of sound, which are vital for shock formation and momentum transfer-a real-gas equation is utilized. Property tables based on the NIST REFPROP database were integrated into Simcenter FloEFD to ensure physically consistent evaluations of pressure–temperature–density relationships across the entire flow field. This approach provides a much more reliable estimation of flow characteristics, such as shock position, jet core persistence, and entrainment ratio, especially under conditions near the critical point or saturation.

$$P(\rho, T) = \rho R T\left[1 + \delta\left(\frac{\partial \alpha^r}{\partial \delta}\right)_\tau\right] \tag{7}$$

Here, α^r residual part of the reduced Helmholtz free energy, δ is the reduced density, and τ is the inverse reduced temperature [36].

2.3. Turbulence Modeling (k–ω-Based SST Formulation)

The interaction between shocks, shear layers, and turbulence amplification mechanisms governs mixing and pressure recovery within a supersonic ejector; therefore, the k–ω-based SST turbulence model and advanced wall functions implemented in Simcenter FloEFD were utilized to represent this complex structure accurately. This approach combines k–ω behavior near the walls with k–ε characteristics in the free stream, providing robust results for compressible flows involving shocks, separation, and strong shear. The two-layer wall model ensures automatic adaptation across fine and coarse meshes, while local refinements at the nozzle exit and mixing chamber walls maintain y^+ values within an appropriate range to capture shock–boundary layer interactions. Considering the high computational cost of detailed methods like LES or DES, the SST-based RANS approach offers the most effective balance between computational efficiency and physical realism for investigating steady-state performance trends.

Turbulent kinetic energy (k) equation:

$$\frac{\partial(\rho k)}{\partial t} + \frac{\partial(\rho k u_i)}{\partial x_i} = \tilde{P}_k - \beta^* \rho k \omega + \frac{\partial}{\partial x_i}\left[(\mu + \sigma_k \mu_t)\frac{\partial k}{\partial x_i}\right] \tag{8}$$

Specific dissipation rate (omega) equation:

$$\frac{\partial(\rho \omega)}{\partial t} + \frac{\partial(\rho \omega u_i)}{\partial x_i} = \alpha \frac{\omega}{k} P_k - \beta \rho \omega^2 + \frac{\partial}{\partial x_i}\left[(\mu + \sigma_\omega \mu_t)\frac{\partial \omega}{\partial x_i}\right] + 2(1 - F_1)\rho \sigma_{\omega 2}\frac{1}{\omega}\frac{\partial k}{\partial x_i}\frac{\partial \omega}{\partial x_i} \tag{9}$$

3. Numerical Setup and Geometry

This section presents a comprehensive framework for the three-dimensional numerical model of the R134a-driven ejector, including the geometric reconstruction process, the sinusoidal mixing chamber design approach, the mesh structure, and the boundary conditions used in the CFD analyses.

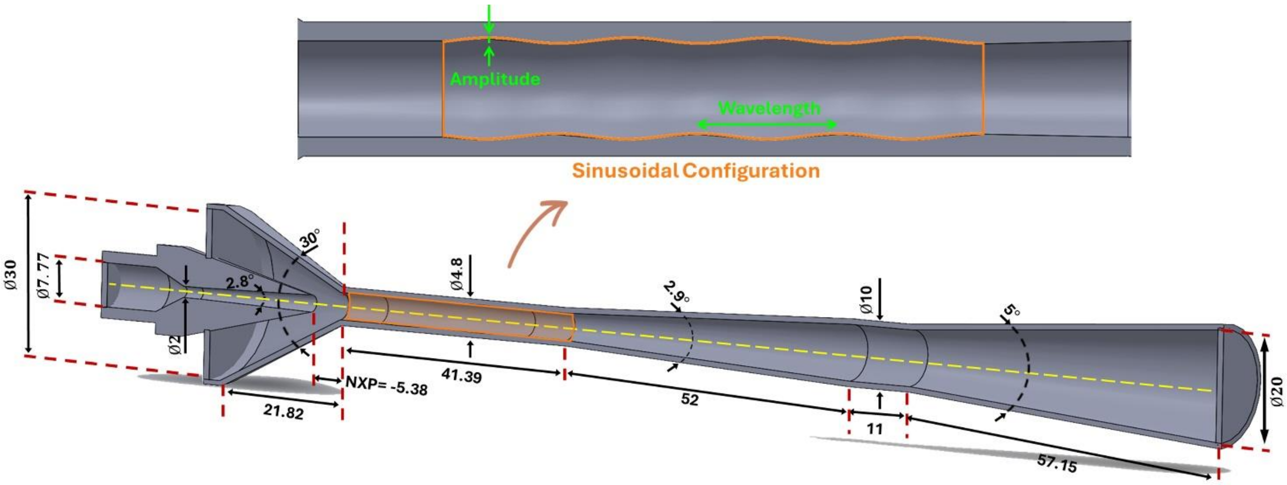

Fig. 1. Main dimensions and geometric parameters of the supersonic ejector used in the present simulations (adapted from [33]).

3.1. Geometry Definition and CAD Modeling

As shown in Fig. 1, the ejector geometry used in this study was reconstructed in a CAD environment based on the supersonic ejector experimentally investigated by Garcia del Valle et al. (2014) [33], consisting of a primary nozzle, suction chamber, constant-area mixing chamber, and diffuser. While the baseline configuration utilizes a circular cross-section mixing chamber, sinusoidal wave forms were derived by adding different amplitudes and wavelengths to the mixing chamber walls. The mean cross sectional area of the mixing chamber was preserved across the sinusoidal configurations. Therefore, the comparison reduces the influence of global flow area variation, although local curvature, wall slope, wetted surface effects, and wall induced vortex generation remain part of the geometric forcing mechanism.

3.2. Sinusoidal Mixing Chamber Design and Equal-Area Constraint

The internal radius of the sinusoidally modified section of the mixing chamber is defined by a mean radius and a dimensionless sinusoidal modulation as follows:

$$R(x) = R_{\text{mean}}\left[1 + A^{*}sin\left(2\pi\frac{x/D_m}{P^{*}}\right)\right], \quad 0 \le x \le L_{wavy} \tag{10}$$

$$A^{*} = \frac{A}{D_m}, P^{*} = \frac{P}{D_m} \tag{11}$$

where $R(x)$ is the axial radius distribution in the sinusoidally modified section, Rmean is the adjusted mean radius, A^{*} is the dimensionless sinusoidal amplitude, P^{*} is the dimensionless wavelength, D_m is the reference mixing chamber diameter, and L_{wavy} is the sinusoidally modified length of the mixing chamber.

The equal area condition was imposed by preserving the average cross sectional area over the sinusoidally modified section:

$$\frac{1}{L_{wavy}}\int_{0}^{L_{wavy}} \pi R^{2}(x)\, dx = \pi R_0^2 \tag{12}$$

where R_0 is the radius of the baseline cylindrical mixing chamber. In this formulation, R_{mean} was adjusted so that the mean cross sectional area of the sinusoidally modified section remained equal to that of the baseline configuration. The straight circular inlet and outlet sections were excluded from this integral because their radius is identical to that of the baseline mixing chamber.

Additionally, straight circular sections with a length of $1.5D_m$ were retained at the inlet and outlet of the sinusoidally modified mixing chamber. These sections were introduced to avoid artificial disturbances near the nozzle exit and to isolate the effect of sinusoidal modulation on the jet wall interaction.

3.3. Boundary Conditions and Working-Fluid Properties

The numerical simulations were performed under operating conditions consistent with those reported by Garcia del Valle et al. [33] in order to enable direct validation and meaningful comparison. The imposed boundary conditions are summarized as follows:

- **Primary flow (boiler inlet):**
  Total pressure $P_g = 2891$ kPa, total temperature $T_g = 94.39\ °C$, corresponding to superheated vapor conditions.

- **Secondary flow (evaporator inlet):**
  Total pressure $P_e = 572.1$ kPa, total temperature $T_e = 20.00$°C.

- **Outlet (condenser):**
  Static pressure, $P_c = 815.9$ kPa, which was imposed consistently with the validated operating condition for the comparative assessment of the baseline and sinusoidal mixing chamber configurations.

R134a was selected as the working fluid. To accurately capture compressible expansion behavior and thermophysical property variations, a real-gas property table derived from the NIST REFPROP database was implemented within the solver.

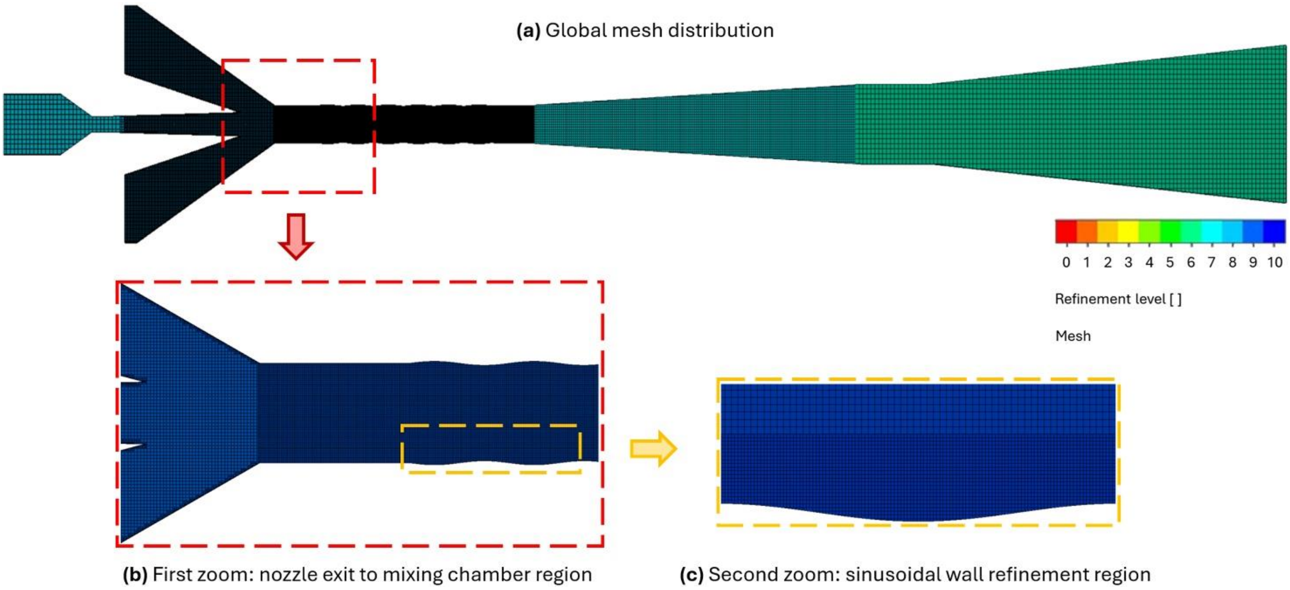

Fig. 2. Multi level mesh refinement strategy used in the numerical model. **(a)** Global mesh distribution of the ejector domain. **(b)** Zoomed view of the nozzle exit and mixing chamber entrance. **(c)** Zoomed view of the sinusoidally modified wall region. Local refinements were applied in these regions to resolve shock structures, shear layer development, and wall induced gradients.

3.4. Mesh Strategy and Local Refinement

To accurately resolve shocks, shear layers, and vortices induced by the sinusoidal walls, a Cartesian finite volume mesh strategy with local refinement regions was used in Simcenter FloEFD. The refinement was not distributed uniformly over the entire computational domain. Instead, local mesh concentrations were applied in the physically critical regions, particularly near the primary nozzle exit, the shock interaction zone, the shear layer development region, and the sinusoidally modified mixing chamber wall.

This strategy was selected because the ejector flow contains strong compressibility effects, rapid pressure gradients, shock boundary layer interactions, and wall induced vortex structures. In the sinusoidal configurations, additional local refinement was applied near the wall crests and troughs to reduce numerical diffusion and to better resolve the geometric forcing imposed by the wavy wall.

The multi level mesh visualization in Fig. 2 demonstrates the increased local resolution applied in the regions where shock structures, shear layer growth, and wall induced gradients are expected to dominate the flow field.

3.5. Mesh Independence Study

The mesh independence study was performed for Case 4 because it represents the shortest wavelength configuration among the wavelength varied cases and therefore imposes strong local curvature and wall induced gradients. The total number of computational cells was systematically increased from approximately 0.7 million to 5,726,554 cells to evaluate the sensitivity of the entrainment ratio to mesh refinement. As shown in Fig. 3, the entrainment ratio approached an asymptotic value as the mesh was refined, and the relative change became lower than 1% at and beyond approximately 3.6 million cells. Therefore, the mesh with 3,658,401 computational cells was selected as the final mesh for the subsequent simulations, while the finest mesh with 5,726,554 cells was used only as a refinement check. Since Simcenter FloEFD uses a Cartesian finite volume discretization, the primary mesh quantity reported by the solver is the number of computational cells. Therefore, the total cell count is reported as the effective finite volume cell count, whereas a separate finite element type node count is not used as a primary mesh reporting metric in the solver output.

Local refinements were mainly focused on physically critical regions, including the nozzle exit, shock interaction zones, the shear layer development region, and the sinusoidally modified mixing chamber wall. This refinement strategy ensured that the high gradient regions governing shock structures, shear layer growth, and wall induced vortex formation were resolved with sufficient local resolution while avoiding unnecessary refinement over the entire computational domain.

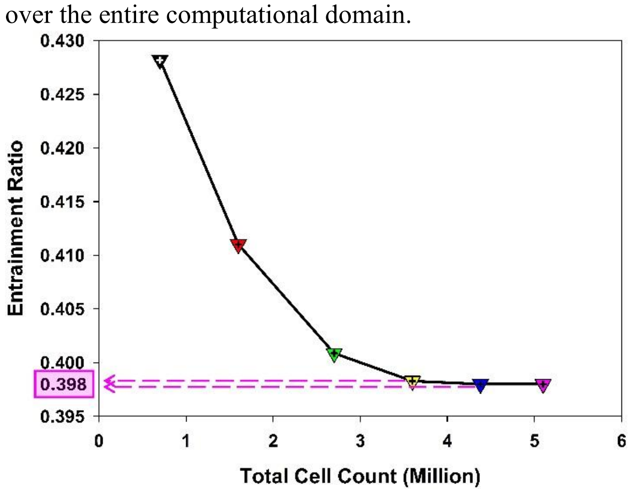

Fig. 3. Mesh independence assessment for Case 4 based on the entrainment ratio as a function of total computational cell count.

3.6. Validation

The numerical model was validated by comparing the baseline ejector results with the experimental entrainment ratios reported by Garcia del Valle et al [33]. The validation was performed for different nozzle exit positions under the same operating conditions used in the reference experiment. The entrainment ratio was selected as the validation metric because it represents the combined effect of primary jet expansion, secondary flow entrainment, shock formation, mixing, and pressure recovery.

The quantitative validation results are summarized in Table 1 and visualized in Fig. 4. The relative error was calculated as the absolute difference between the numerical and experimental entrainment ratios divided by the experimental value.

$$\text{Relative error (\%)} = \frac{|ER_{CFD} - ER_{exp}|}{ER_{exp}} \times 100 \qquad (13)$$

The numerical model reproduced the experimental trend over the investigated nozzle exit positions. The maximum relative deviation was 4.24%, while the mean relative deviation was 3.53%. This level of agreement is acceptable for a three dimensional RANS based supersonic ejector simulation, especially considering the sensitivity of shock location, mixing layer development, and real fluid property variation to geometric and operating conditions. Therefore, the validated baseline model provides a reliable basis for the subsequent investigation of sinusoidally modified mixing chamber geometries.

Table 1. Validation of the baseline ejector model against experimental data from Garcia del Valle et al. [33].

NXP, mm	Experimental ER	CFD ER	Absolute error	Relative error, %
−17.60	0.269592	0.278980	0.009388	3.48
−14.93	0.310748	0.321224	0.010476	3.37
−10.95	0.371293	0.387041	0.015748	4.24
−5.64	0.392721	0.404184	0.011463	2.92
−0.27	0.408027	0.422857	0.014830	3.63

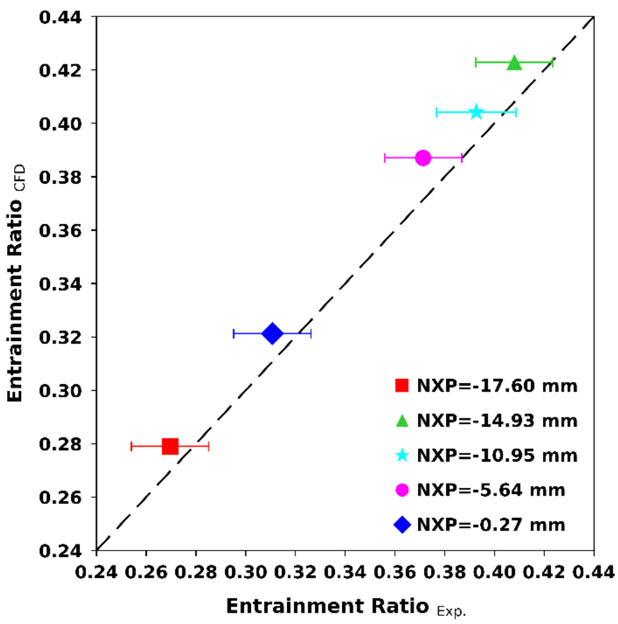

Fig. 4. Validation of the baseline ejector model through comparison between numerical and experimental entrainment ratios for different nozzle exit positions.

3.7. Convergence Monitoring and Numerical Acceptance Criteria

The convergence of each CFD simulation was monitored using both solver based criteria and engineering goal based quantities. In addition to the residual behavior, the primary mass flow rate, secondary mass flow rate, outlet mass flow rate, entrainment ratio, mass imbalance, and outlet static pressure were tracked throughout the calculations. A solution was accepted only when the monitored engineering quantities reached stable final values and no further displacement of the dominant shock structures was observed.

For the representative Case 4 simulation, the mass flow rate based goals, entrainment ratio, and mass imbalance reached their convergence criteria between iterations 358 and 504. However, the calculation was continued until 4.00204 travels were completed. This additional continuation was used to verify the persistence of the converged solution, to reduce the risk of premature goal stabilization, and to ensure that the shock structure, pressure field, and mass balance behavior did not exhibit delayed numerical drift after the first achievement of the goal criteria. The outlet static pressure was monitored as an auxiliary pressure field indicator, whereas the primary convergence assessment was based on the stabilization of mass flow rates, entrainment ratio, and mass imbalance. The convergence monitoring quantities and numerical acceptance indicators for the representative Case 4 simulation are summarized in Table 2.

Table 2. Convergence monitoring and numerical acceptance criteria for the representative Case 4 simulation.

Monitored quantity	Final value	Convergence indicator
Total computational cells	3,658,401	Final mesh level
Fluid cells contacting solid boundaries	1,440,408	Near wall refinement indicator
Iterations	1,432	Solver completed
Travels	4.00204	Solver completed
Primary mass flow rate	2.58079×10^{-5} kg/s	Achieved at iteration 358
Secondary mass flow rate	9.03375×10^{-6} kg/s	Achieved at iteration 358
Outlet mass flow rate	-3.387014×10^{-5} kg/s	Achieved at iteration 504
Entrainment ratio, ER	0.35012	Achieved at iteration 358
Mass imbalance	2.78836%	Achieved at iteration 470
Outlet static pressure	815,586 Pa	Achieved at iteration 622

4. Results and Discussions

In this section, the 3D CFD results for the supersonic ejector configurations with sinusoidally modified mixing chambers are presented and compared in detail. Mach number and turbulent kinetic energy (TKE) contours are evaluated alongside axial distributions. The effects of A^* and P^* parameters are analyzed through both contour plots

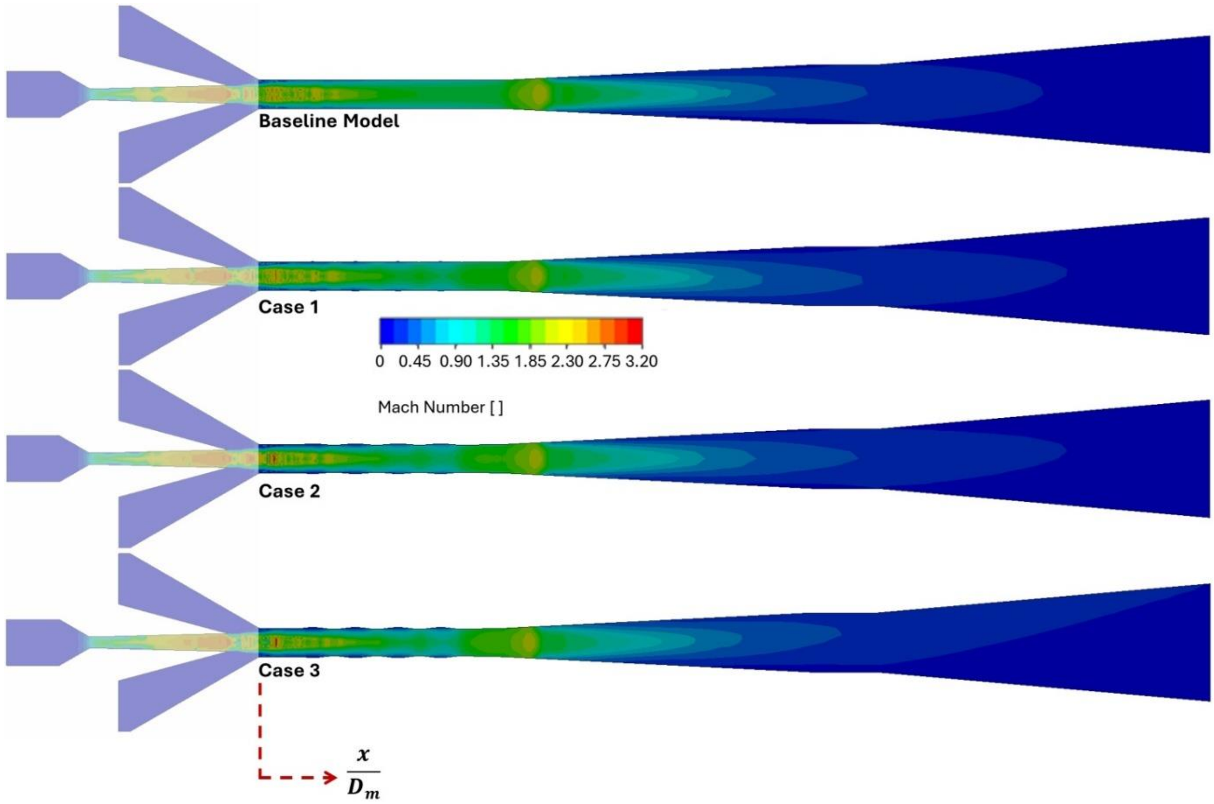

Fig. 5. Mach number contours in the mixing chamber for the baseline and sinusoidal cases with varying dimensionless amplitude A^*(constant $P^* = 1.5$).

4.1. Flow Structure and Jet Development

Mach number contours for the baseline and sinusoidally modified models are presented in Figs. 5 and 6. Including the baseline model in both sets allows for a direct visual comparison of how sinusoidal geometries alter the flow. The baseline model maintains a classic supersonic jet structure characterized by a long potential core and regular shock cells.

Figure 5 illustrates the effect of sinusoidal amplitude (A^*) on the Mach field. This visualization reveals that increasing wall waviness intensifies streamwise vortices and destabilizes the shock cell structure, leading to an earlier collapse of the supersonic potential core. As amplitude increases, the jet core fails over a shorter axial distance. Compared to the baseline, the systematic shortening of Mach > 1 regions from Case 1 to Case 3 reflects the increasing impact of geometric forcing imposed by the A^* parameter. The general trend indicates that heightened wall waviness progressively weakens the axial integrity of the jet and reduces stability as amplitude increases.

Figure 6 shows the effect of wavelength (P^*) on the Mach field. It is observed that in Case 4, which has a short wavelength, the jet dissipates rapidly compared to the baseline; conversely, in Case 6, with a longer wavelength, the potential core is more steadily preserved. Short wavelengths impose high-frequency geometric forcing that disrupts the jet quickly, while longer wavelengths create a more organized and gentler forcing, allowing for more regular vortex development. This prevents the abrupt breakdown of the shock structure, maintaining the supersonic core for a longer duration. Thus, the general trend is that the jet retains its supersonic character longer as P^* increases. These findings highlight the critical role of P^* in balancing jet destabilization and momentum conservation.

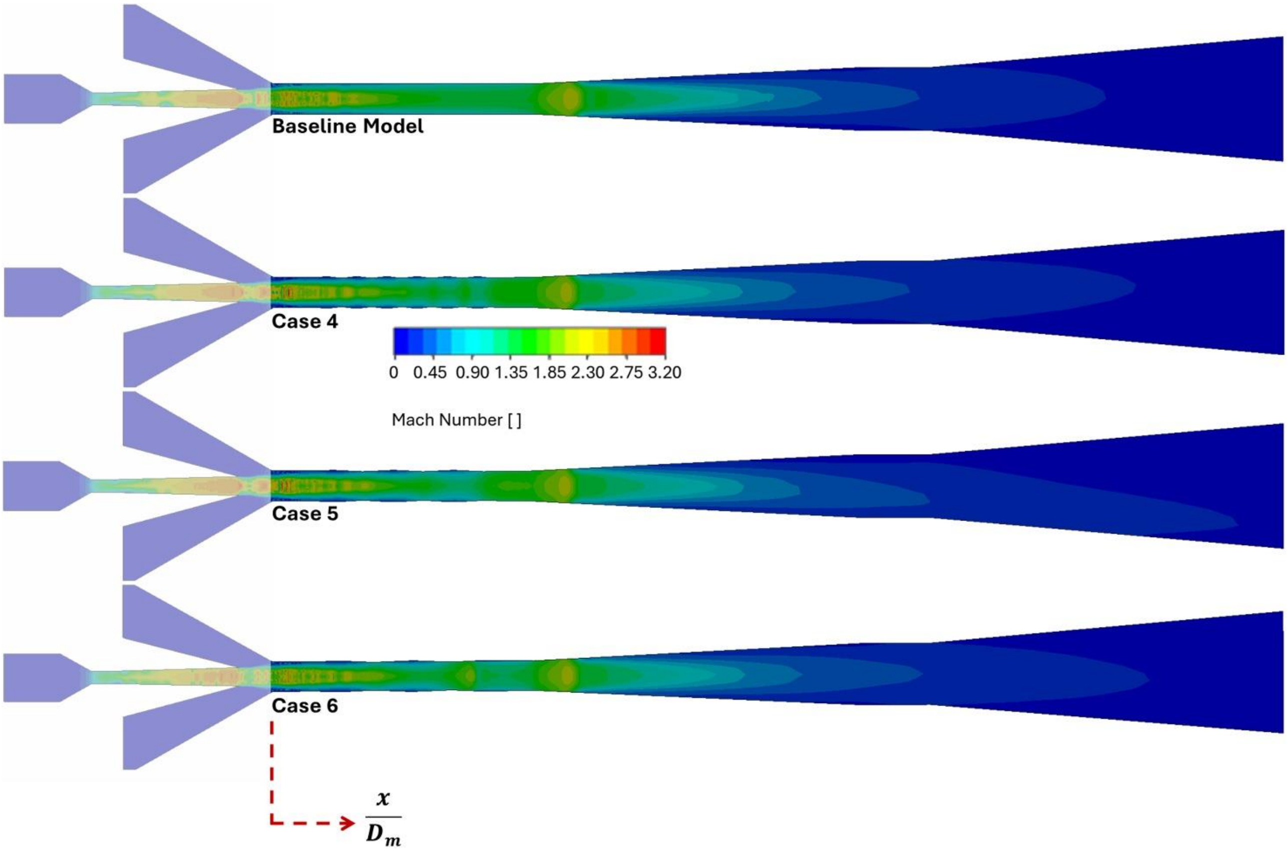

Fig. 6. Mach number contours in the mixing chamber for the baseline and sinusoidal cases with varying dimensionless wavelength P^*(constant $A^* = 0.02$).

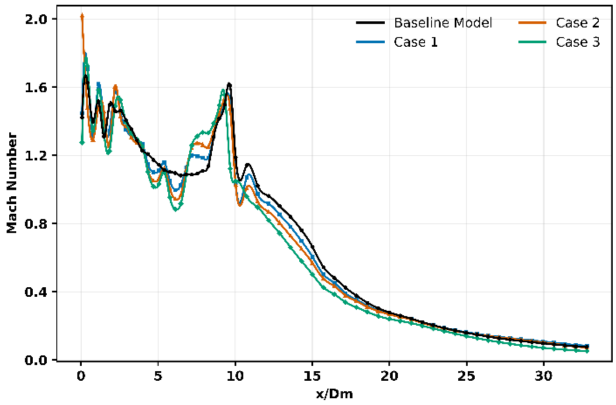

Fig. 7. Centerline Mach number distributions for different dimensionless amplitudes A*, illustrating the effect of sinusoidal wall strength on jet core decay.

Figure 7 presents the Mach number distribution along the centerline for different A^* values. This graph quantitatively confirms that as amplitude increases, the Mach drop shifts to earlier axial positions (upstream) and the potential core shortens monotonically. The axial reduction in Mach number proves that stronger sinusoidal wall modulation accelerates shock breakdown and jet spreading. While the general curve characteristics are similar across all cases, it is evident that the downward break in Mach curves occurs earlier as amplitude increases. These quantitative data align closely with the Mach number contours shown in Figure 5.

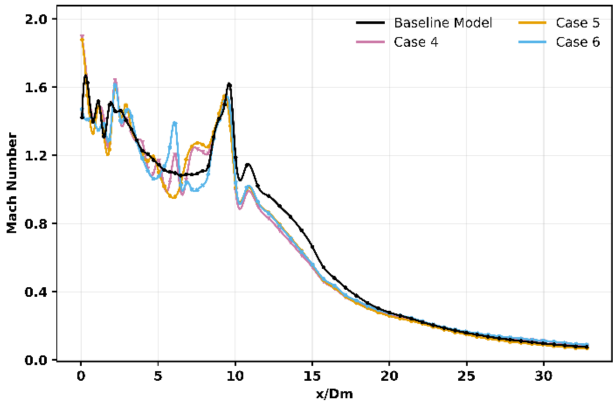

Fig. 8. Centerline Mach number distributions for different dimensionless wavelengths P*, showing the influence of geometric forcing frequency on jet stability.

Figure 8 shows the influence of wavelength (P^*) variation on axial Mach profiles. Case 6, with its longer wavelength, exhibits a more prolonged supersonic core structure than Case 4. The preservation of high Mach numbers over a greater distance in long-wavelength cases indicates a more gradual and controlled modulation of the jet. This demonstrates that wavelength is a control parameter that is at least as critical as amplitude for jet stability. This trend indicates that increasing P^*generally delays the collapse of the supersonic core and promotes a more gradual jet decay. However, the entrainment response is not strictly monotonic. Increasing P^* from 1.0 to 2.0 improves the entrainment ratio, whereas a further increase to $P^* = 2.5$ preserves a more controlled flow structure but does not provide the maximum ER.

4.2. Turbulence Production and Energy Distribution

Turbulent kinetic energy (TKE) contours are presented in two separate sets in Figs. 9 and 10, whereas the corresponding centerline TKE distributions are shown in Figs. 11 and 12. This allows for a direct observation of how sinusoidal geometries modify turbulence production relative to the baseline configuration. In both contour sets, the baseline model is characterized by low TKE levels at the mixing chamber inlet and a rising turbulence field in the region where the jet naturally collapses.

Figure 9 displays the effect of sinusoidal amplitude (A^*) on TKE fields. As amplitude increases, TKE levels rise significantly, and the turbulent regions advance toward the mixing chamber inlet (upstream). This indicates that as wall-induced vortices strengthen and shear layer interactions increase, mean flow energy is converted more rapidly into turbulent fluctuations. While this intensified turbulence accelerates mixing, it also promotes momentum loss. The common trend across all cases is a systematic increase in turbulence production and mixing intensity as A^* increases.

Figure 10 illustrates the impact of wavelength (P^*) on the TKE field. In Case 4 (short wavelength), turbulence energy is concentrated at the mixing chamber inlet, whereas in Case 6 (long wavelength), TKE is distributed over a broader axial area. This spatial redistribution explains why long-wavelength cases achieve a more successful balance between mixing and momentum conservation. Longer wavelengths distribute turbulence energy more homogeneously along the flow, limiting abrupt momentum losses and enhancing flow stability.

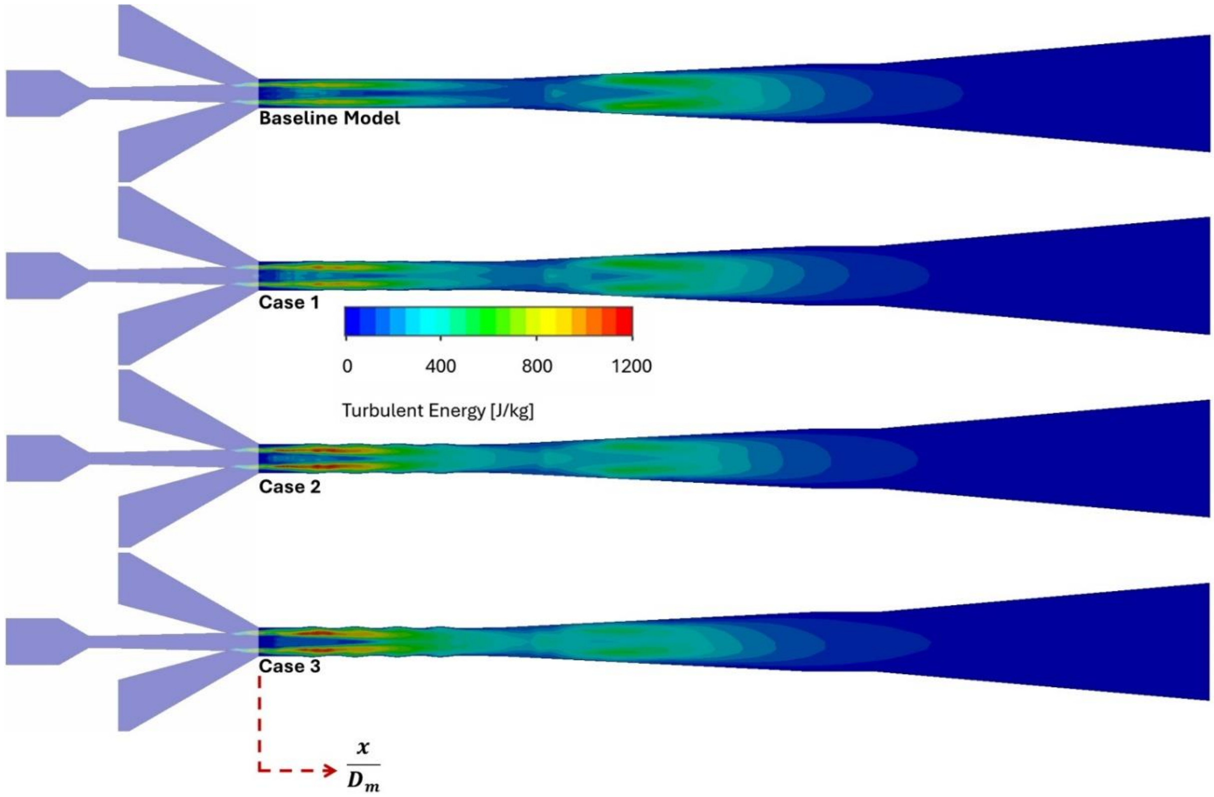

Fig. 9. Turbulence kinetic energy (TKE) contours in the mixing chamber for the baseline and sinusoidal cases with varying dimensionless amplitude A^*(constant $P^* = 1.5$).

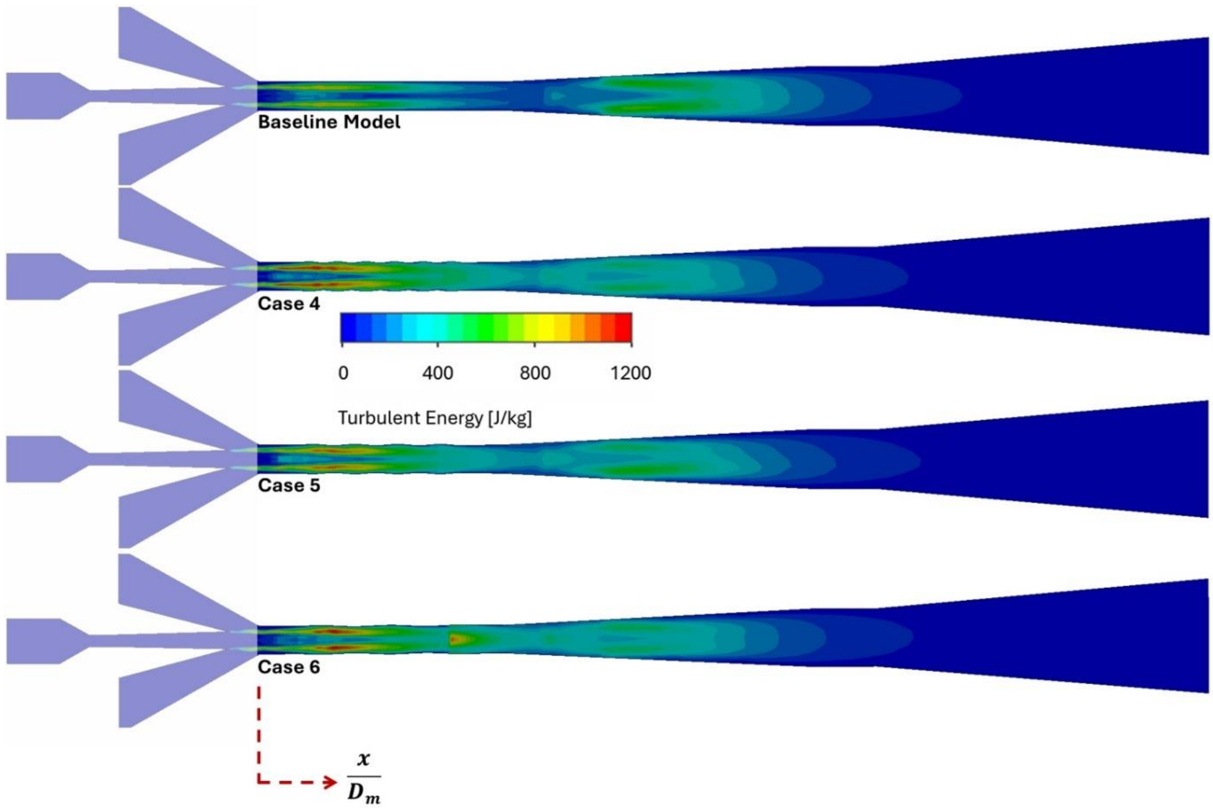

Fig. 10. Turbulence kinetic energy (TKE) contours in the mixing chamber for the baseline and sinusoidal cases with varying dimensionless wavelength P^*(constant $A^* = 0.02$).

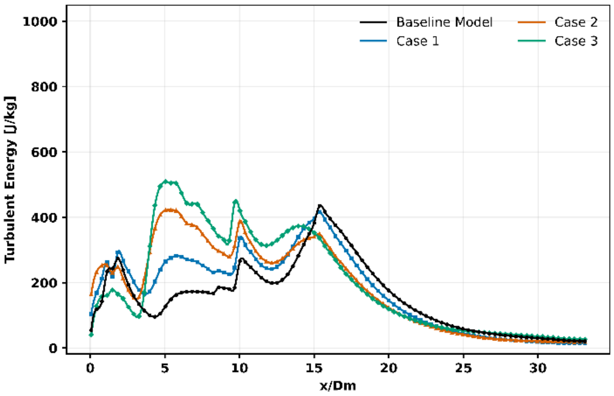

Fig. 11. Centerline turbulence kinetic energy distributions for different dimensionless amplitudes A*, highlighting the impact of wall waviness on turbulence production.

Figure 11 presents TKE variation along the centerline for different A^* values. This graph quantitatively confirms that peak TKE values rise and shift toward earlier axial positions (upstream) as amplitude increases. The upstream shift of these peaks demonstrates an intensifying energy transfer from the mean flow to turbulence. This physical change proves that amplitude is the primary parameter determining mixing intensity. This trend is also directly related to the drop in entrainment ratio observed at high amplitudes. These data show high agreement with the TKE contours in Figure 9.

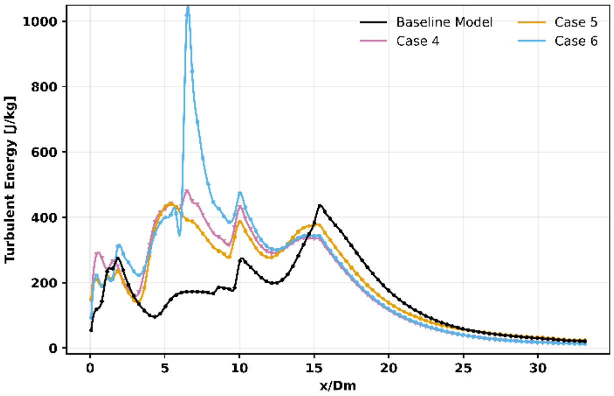

Fig. 12. Centerline turbulence kinetic energy distributions for different dimensionless wavelengths P*, illustrating the role of wavelength in controlling energy redistribution.

Figure 12 shows the effect of wavelength (P^*) variation on axial TKE profiles. Long-wavelength cases exhibit a more diffused and moderate TKE profile by spreading energy over a larger distance, while short wavelengths produce sharp, localized peaks. This difference in spatial distribution demonstrates that long wavelengths prevent sudden energy loss and create a more controlled mixing zone. This is the fundamental physical mechanism explaining why larger P^* values promote smoother TKE redistribution and reduce abrupt jet breakdown. However, the entrainment response is not strictly monotonic, and the maximum entrainment ratio among the wavelength varied sinusoidal cases occurs at the intermediate wavelength.

Table 3. Dimensionless sinusoidal geometry parameters of the mixing chamber (A*, P*, and Ψ) for all investigated cases.

Case	A*	P*	Ψ = A*/P*	Physical Regime
Baseline	0	–	-	Smooth cylindrical wall
Case 1	0.01	1.5	0.0067	Weak vortex generation
Case 2	0.02	1.5	0.0133	Active SWBLI regime
Case 3	0.03	1.5	0.0200	Excessive vortexing and jet breakdown
Case 4	0.02	1.0	0.0200	High-frequency wall forcing
Case 5	0.02	2.0	0.0100	Moderate modulation
Case 6	0.02	2.5	0.0080	Long-wave, controlled vortex generation

4.3. Effect on Entrainment Performance

The impact of these observed changes in Mach and TKE fields on global performance is evaluated using the entrainment ratio, ER, and wall-integrated friction forces (F_f) provided in Table 4.

Table 4. Performance summary of the baseline and sinusoidal ejector configurations.

Case	*ER*	Observed TKE Trend	F_f *(N)*	Flow Regime
Baseline	0.398	Low with late rise	0.308	Long jet core
Case 1	0.388	Moderate	0.343	Moderate vortex generation
Case 2	0.358	High	0.323	Strong SWBLI
Case 3	0.322	Very high	0.300	Excessive turbulent mixing
Case 4	0.350	High with inlet peak	0.308	High frequency forcing
Case 5	0.368	Balanced	0.323	Moderate wavelength mixing
Case 6	0.359	Balanced and diffused	0.339	Controlled long wavelength mixing

The baseline model yields the highest entrainment ratio, ER = 0.398, while increasing the amplitude at a constant wavelength from Case 1 to Case 3 leads to a systematic decline in ER. The ER value decreases from 0.388 in Case 1 to 0.322 in Case 3. This indicates that increased wall waviness redirects part of the primary jet momentum into turbulent fluctuations rather than preserving it for secondary flow entrainment. Consequently, stronger mixing does not always translate into better ejector performance.

Under constant amplitude conditions ($A^* = 0.02$), the wavelength effect is not strictly monotonic in terms of entrainment ratio. Increasing P^* from 1.0 to 2.0 improves ER from 0.350 in Case 4 to 0.368 in Case 5, indicating that a moderate wavelength reduces premature jet breakdown and supports more effective momentum transfer. However, a further increase to P^* = 2.5 in Case 6 decreases ER slightly to 0.359, although the flow field remains more controlled and less abruptly destabilized than in the short wavelength case. Therefore, Case 5 provides the maximum ER among the wavelength varied cases, whereas Case 6 represents a more diffused and controlled mixing regime. These results indicate that wavelength governs the balance between jet destabilization and momentum conservation, but larger P^* values should not be interpreted as automatically improving entrainment performance.

4.4. Wall Friction and Energy Losses

The wall integrated friction forces (F_f) in Table 4 further clarify the performance trends. The friction force does not increase monotonically with sinusoidal modulation. Some sinusoidal cases show friction levels comparable to or slightly lower than the baseline, indicating that the entrainment loss cannot be attributed to wall friction alone. For example, Case 3 has a friction force close to the baseline but exhibits the lowest entrainment ratio. This shows that performance loss is governed primarily by internal turbulence production and momentum redistribution rather than by wall friction alone. In contrast, the long wavelength cases distribute turbulence more smoothly along the mixing chamber, which explains their more controlled flow behavior.

4.5. General Evaluation

When Mach and TKE contours, centerline profiles, and quantitative metrics are evaluated together, it is clear that the sinusoidal mixing chamber fundamentally alters the interaction among shocks, vortices, and turbulence. While excessive geometric forcing rapidly consumes jet momentum, controlled combinations of wavelength and amplitude can promote early mixing while limiting abrupt momentum loss. In terms of entrainment ratio, Case 5 provides the most favorable sinusoidal configuration. Case 6, however, represents a more controlled long wavelength mixing regime with smoother turbulence and momentum redistribution.

5. Conclusions

In this study, the effects of sinusoidally modified mixing chambers on the flow structure and performance of an R134a driven supersonic ejector were comprehensively investigated through three dimensional numerical analyses. By preserving the mean cross sectional area and systematically varying the dimensionless amplitude, A^*, and wavelength, P^*, the influence of wall induced geometric forcing on shock dynamics, turbulence production, and entrainment performance was evaluated.

The CFD results show that sinusoidal wall modulation substantially modifies the internal flow physics of the ejector. Periodic wall curvature promotes streamwise vortex formation and shock wave and boundary layer interactions, which accelerate the collapse of the supersonic potential core and enhance the mixing between the primary and secondary streams. However, excessive geometric forcing redirects a considerable portion of the primary jet momentum into turbulent kinetic energy, which reduces the entrainment ratio. Therefore, stronger mixing does not necessarily correspond to better ejector performance.

At a constant wavelength of P^*=1.5, increasing the amplitude from A^*=0.01 to A^*=0.03 systematically increased turbulence intensity and caused a significant reduction in entrainment performance. This result indicates that aggressive wall waviness intensifies mixing but also produces excessive momentum dissipation. Consequently, high amplitude modulation is not energetically favorable for the present ejector configuration.

At a constant amplitude of A^* = 0.02, the effect of wavelength was not strictly monotonic. Increasing P^* from 1.0 to 2.0 improved the entrainment ratio, with Case 5 providing the highest ER among the sinusoidal configurations. However, a further increase to P^* = 2.5 did not further improve ER. Instead, Case 6 produced a more controlled and spatially distributed mixing regime. This shows that the preferred wavelength depends on whether the design objective prioritizes maximum entrainment or smoother momentum redistribution.

The dimensionless forcing parameter Ψ provides a useful first order indicator for interpreting the intensity of geometric forcing. Large Ψ values are generally associated with excessive vortex generation, rapid jet breakdown, and reduced entrainment performance. Lower Ψ values tend to reduce overly aggressive turbulence production. However, Ψ should not be interpreted as a unique performance similarity parameter, because amplitude, wavelength, wall slope, and curvature can produce different flow responses even at comparable Ψ values.

Overall, the smooth baseline configuration provides the highest entrainment ratio under the investigated operating condition. Among the sinusoidal configurations, Case 5 represents the most favorable design in terms of entrainment ratio, whereas Case 6 represents a more controlled mixing regime with smoother redistribution of turbulence and momentum. These findings provide a dimensionless basis for interpreting sinusoidal mixing chamber designs and may guide future parametric studies involving broader ejector geometries, working fluids, and operating conditions.

Nomenclature

Latin symbols

Symbol	Description	Unit
A	Sinusoidal amplitude	m
A^*	Dimensionless sinusoidal amplitude	-
A_e	Nozzle exit area	m²
A_{ne}	Nozzle exit area used in the one dimensional ejector relation	m²
A_t	Nozzle throat area	m²
D_m	Reference mixing chamber diameter	m
ER	Entrainment ratio	-
F_f	Wall integrated friction force	N
F_1	SST blending function	-
h	Specific enthalpy	J/kg
H	Total enthalpy	J/kg
k	Turbulent kinetic energy	m²/s²
L_{wavy}	Sinusoidally modified length of the mixing chamber	m
Ma	Mach number	-
Ma_{ne}	Nozzle exit Mach number	-
M_e	Exit Mach number	-
$\dot{m}_p$	Primary mass flow rate	kg/s
P	Sinusoidal wavelength	m
P^*	Dimensionless sinusoidal wavelength	-
p	Static pressure	Pa
P_c	Condenser outlet pressure	Pa
P_e	Secondary inlet pressure	Pa
P_g	Primary inlet pressure	Pa
Pr	Molecular Prandtl number	-
Pr_t	Turbulent Prandtl number	-
R	Gas constant	J/kg K
$R(x)$	Axial radius distribution of the sinusoidal mixing chamber	m
R_0	Reference radius	m
R_{mean}	Mean radius of the sinusoidal mixing chamber	m
T	Temperature	K
T_e	Secondary inlet temperature	K
T_g	Primary inlet temperature	K
u_i	Velocity component in the x_i direction	m/s
x	Axial coordinate	m
x_i	Cartesian coordinate	m
y^+	Dimensionless wall distance	-

Greek symbols

Symbol	Description	Unit
α^r	Residual part of the reduced Helmholtz free energy	-
β	Model coefficient in the specific dissipation rate equation	-
β^*	Model coefficient in the turbulent kinetic energy equation	-
γ	Specific heat ratio	-
δ	Reduced density	-
μ	Dynamic viscosity	Pa s
μ_t	Turbulent viscosity	Pa s
ρ	Density	kg/m³
σ_k	Turbulent Prandtl coefficient for k	-
σ_ω	Turbulent Prandtl coefficient for ω	-
$\sigma_{\omega 2}$	Cross diffusion coefficient in the SST formulation	-
τ	Inverse reduced temperature	-
τ_{ij}	Viscous stress tensor	Pa
ω	Specific dissipation rate	1/s
Ψ	Dimensionless geometric forcing parameter, A^*/P^*	-

Abbreviations

Symbol	Description
CAD	Computer aided design
CFD	Computational fluid dynamics
EOS	Equation of state
NIST REFPROP	National Institute of Standards and Technology Reference Fluid Thermodynamic and Transport Properties database
NXP	Nozzle exit position
RANS	Reynolds averaged Navier Stokes
SST	Shear stress transport
SWBLI	Shock boundary layer interaction
TKE	Turbulent kinetic energy

References

[1] P. Haghparast, M. V. Sorin, and H. Nesreddine, "The impact of internal ejector working characteristics and geometry on the performance of a refrigeration cycle," *Energy*, vol. 162, pp. 728–743, 2018, doi: 10.1016/j.energy.2018.08.017.

[2] D. Duan, H. Ge, X. Xi, and B. Zhang, "Performance and mixing process investigation of a novel mixing-enhanced ejector," *Sustain. Energy Technol. Assessments*, vol. 58, no. June, p. 103322, 2023, doi: 10.1016/j.seta.2023.103322.

[3] Z. Aidoun and M. Ouzzane, "The effect of operating conditions on the performance of a supersonic ejector for refrigeration," *Int. J. Refrig.*, vol. 27, no. 8, pp. 974–984, 2004, doi: 10.1016/j.ijrefrig.2004.05.006.

[4] A. R. Srikrishnan, J. Kurian, and V. Sriramulu, "Experimental study on mixing enhancement by petal nozzle in supersonic flow," *J. Propuls. Power*, vol. 12, no. 1, pp. 165–169, 1996, doi: 10.2514/3.24006.

[5] G. Al-Doori, K. Saleh, A. Al-Manea, R. Al-Rbaihat, Y. Altork, and A. Alahmer, "A review of axial and radial ejectors: Geometric design, computational analysis, performance, and machine learning approaches," *Appl. Therm. Eng.*, vol. 266, no. January, p. 125694, 2025, doi: 10.1016/j.applthermaleng.2025.125694.

[6] S. Kim and S. Kwon, "Experimental determination of geometric parameters for an annular injection type supersonic ejector," *J. Fluids Eng. Trans. ASME*, vol. 128, no. 6, pp. 1164–1171, 2006, doi: 10.1115/1.2353264.

[7] M. Hamzaoui, H. Nesreddine, and Z. Aidoun, "A Numerical and Experimental Performance Assessment of a Single-Phase Supersonic Ejector," *Arab. J. Sci. Eng.*, vol. 47, no. 7, pp. 8899–8913, 2022, doi: 10.1007/s13369-021-06437-2.

[8] J. Chen, Z. Wang, J. Wu, and W. Xu, "Investigation on the pressure matching performance of the constant area supersonic-supersonic ejector," *Therm. Sci.*, vol. 9, no. 2, pp. 631–643, 2015, doi: 10.2298/TSCI120405114C.

[9] L. Cai, H. T. Zheng, Y. J. Li, and Z. M. Li, "Computational fluid dynamics simulation of the

supersonic steam ejector. Part 2. Optimal design of geometry and the effect of operating conditions on the ejector,” *Proc. Inst. Mech. Eng. Part C J. Mech. Eng. Sci.*, vol. 226, no. 3, pp. 715–723, 2012, doi: 10.1177/0954406211415779.

[10] J. Kracik and V. Dvorak, “Development of an Analytical Method for Predicting Flow in a Supersonic Air Ejector,” *EPJ Web Conf.*, vol. 114, pp. 1–6, 2016, doi: 10.1051/epjconf/201611402059.

[11] X. Yang, X. Long, and X. Yao, “Numerical investigation on the mixing process in a steam ejector with different nozzle structures,” *Int. J. Therm. Sci.*, vol. 56, pp. 95–106, 2012, doi: 10.1016/j.ijthermalsci.2012.01.021.

[12] O. Lamberts, P. Chatelain, and Y. Bartosiewicz, “Numerical and experimental evidence of the Fabri-choking in a supersonic ejector,” *Int. J. Heat Fluid Flow*, vol. 69, no. January, pp. 194–209, 2018, doi: 10.1016/j.ijheatfluidflow.2018.01.002.

[13] J. Kracik and V. Dvorak, “Secondary flow choking in axisymmetric supersonic air ejector with adjustable motive nozzle,” *Appl. Therm. Eng.*, vol. 204, no. November 2021, p. 117936, 2022, doi: 10.1016/j.applthermaleng.2021.117936.

[14] V. Dvorak and P. Safarik, “Transonic instability in entrance part of mixing chamber of high-speed ejector,” *J. Therm. Sci.*, vol. 14, no. 3, pp. 258–264, 2005, doi: 10.1007/s11630-005-0011-5.

[15] Z. Jian-Jun, Z. Jin, L. Hui-Qiang, and H. Yong, “Experimental investigation on starting process of supersonic single-stage air ejector,” *J. Therm. Sci.*, vol. 21, no. 4, pp. 348–353, 2012, doi: 10.1007/s11630-012-0554-1.

[16] J. Dong, X. Wang, and J. Tu, “Numerical Research about the Internal Flow of Steam-jet Vacuum Pump: Evaluation of Turbulence Models and Determination of the Shock-mixing Layer,” *Phys. Procedia*, vol. 32, no. August 2010, pp. 614–622, 2012, doi: 10.1016/j.phpro.2012.03.608.

[17] Y. Shan, J. zhou Zhang, and X. wen Ren, “Numerical modeling on pumping performance of piccolo-tube multi-nozzles supersonic ejector in an oil radiator passage,” *Energy*, vol. 158, pp. 216–227, 2018, doi: 10.1016/j.energy.2018.06.001.

[18] Z. X. Yang, J. Y. Zhang, F. N. Cheng, L. J. Chen, J. X. Geng, and Z. X. Gong, “Numerical study of structural parameters on the performance of piccolo-tube muti-nozzles supersonic ejector in air-cooled passage,” *Case Stud. Therm. Eng.*, vol. 69, no. July 2024, p. 105982, 2025, doi: 10.1016/j.csite.2025.105982.

[19] M. A. Talebiyan, M. Nili-Ahmadabadi, and M. Y. Ha, “Performance enhancement of supersonic ejectors via aerodynamic cavities: A numerical parametric study,” *J. Mech. Sci. Technol.*, vol. 39, no. 1, pp. 259–274, 2025, doi: 10.1007/s12206-024-1225-3.

[20] M. Dandani, V. Lepiller, A. Ghezal, and P. Desevaux, “Numerical visualizations of mixing enhancement in a 2D supersonic ejector,” *Fluid Dyn. Mater. Process.*, vol. 14, no. 1, pp. 23–37, 2018, doi: 10.3970/fdmp.2018.014.023.

[21] Z. Li, Y. Wang, W. Xu, T. Liang, and S. Zhang, “Experimental and Numerical Studies on the Performance and Mixing Characteristics of Supersonic Annular Ejector,” *Heat Transf. Eng.*, vol. 0, no. 0, pp. 1–20, 2025, doi: 10.1080/01457632.2025.2571268.

[22] L. Cai and M. He, “A numerical study on the supersonic steam ejector use in steam turbine system,” *Math. Probl. Eng.*, vol. 2013, pp. 1–10, 2013, doi: 10.1155/2013/651483.

[23] L. Vojta, J. Kracik, and V. Dvorak, “Introductory Numerical Study on Supersonic Ejector Working with R32,” *EPJ Web Conf.*, vol. 213, p. 02096, 2019, doi: 10.1051/epjconf/201921302096.

[24] K. Ariafar, T. Cochrane, R. Malpress, and D. Buttsworth, “Pitot and static pressure measurement and CFD simulation of a co-flowing steam jet,” *Exp. Therm. Fluid Sci.*, vol. 97, no. April, pp. 36–47, 2018, doi: 10.1016/j.expthermflusci.2018.04.004.

[25] L. Zheng, Y. Zhang, L. Hao, H. Lian, J. Deng, and W. Lu, “Modelling, Optimization, and Experimental Studies of Refrigeration CO2 Ejectors: A Review,” *Mathematics*, vol. 10, no. 22, 2022, doi: 10.3390/math10224325.

[26] H. Zhang, L. Wang, L. Jia, H. Zhao, and C. Wang, “Étude De L’Influence De La Friction Sur La Performance D’Un Éjecteur Supersonique,” *Int. J. Refrig.*, vol. 85, pp. 229–239, 2018, doi: 10.1016/j.ijrefrig.2017.09.028.

[27] D. V. Brezgin, K. E. Aronson, F. Mazzelli, and A. Milazzo, “The surface roughness effect on the performance of supersonic ejectors,” *Thermophys. Aeromechanics*, vol. 24, no. 4, pp. 553–561, 2017, doi: 10.1134/S0869864317040060.

[28] J. Kracik and V. Dvorak, “Effect of wall roughness on secondary flow choking in supersonic air ejector with adjustable motive nozzle,” *Int. J. Heat

Fluid Flow, vol. 103, no. June, p. 109168, 2023, doi: 10.1016/j.ijheatfluidflow.2023.109168.

[29] G. Al-Doori, K. Saleh, A. Al-Manea, R. Al-Rbaihat, Y. Altork, and A. Alahmer, "A review of axial and radial ejectors: Geometric design, computational analysis, performance, and machine learning approaches," *Appl. Therm. Eng.*, vol. 266, no. January, p. 125694, 2025, doi: 10.1016/j.applthermaleng.2025.125694.

[30] K. Śmierciew, D. Butrymowicz, J. Karwacki, M. J. Bergander, and J. Gagan, "Design, fabrication, and investigations of prototype supersonic micro-ejector for innovative cooling system of electronic components," *Int. J. Refrig.*, vol. 153, no. May, pp. 323–336, 2023, doi: 10.1016/j.ijrefrig.2023.05.018.

[31] T. Liang, Z. Li, W. Xu, S. Zhang, and W. Ye, "Experimental and numerical studies on the performance of a precooled supersonic ejector," *Appl. Therm. Eng.*, vol. 253, no. June, p. 123823, 2024, doi: 10.1016/j.applthermaleng.2024.123823.

[32] M. Majchrzyk *et al.*, "Detailed numerical investigation of the CO2 two-phase ejector 3-D CFD model based on the flow visualisation experiments," *Chem. Eng. Process. - Process Intensif.*, vol. 182, no. February, p. 109195, 2022, doi: 10.1016/j.cep.2022.109195.

[33] J. García del Valle, J. M. Saíz Jabardo, F. Castro Ruiz, and J. F. San José Alonso, "An experimental investigation of a R-134a ejector refrigeration system," *Int. J. Refrig.*, vol. 46, pp. 105–113, Oct. 2014, doi: 10.1016/j.ijrefrig.2014.05.028.

[34] B. J. Huang, J. M. Chang, C. P. Wang, and V. A. Petrenko, "A 1-D analysis of ejector performance," *Int. J. Refrig.*, vol. 22, no. 5, pp. 354–364, Aug. 1999, doi: 10.1016/S0140-7007(99)00004-3.

[35] F. Kong, Y. Jin, T. Setoguchi, and H. D. Kim, "Numerical Analysis of Chevron Nozzle Effects on Performance of the Supersonic Ejector-Diffuser System," *J. Therm. Sci.*, vol. 22, no. 5, pp. 459–466, 2013, doi: 10.1007/s11630-013-0648-4 Article.

[36] Simcenter, "FloEFD," 2025, *Siemens*: v25.12.